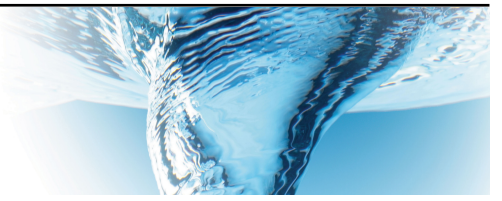
J. Fluid Mech. (2026), *vol.* 1043, R3, doi:10.1017/jfm.2026.12022



Bacterial adhesion to curved surfaces in fluid flow

Edwina F. Yeo[1], **Benjamin J. Walker**[1], **Philip Pearce**[1,2] and **Mohit P. Dalwadi**[1,3]

[1]Department of Mathematics, University College London, London, UK

[2]Institute for the Physics of Living Systems, University College London, London, UK

[3]Mathematical Institute, University of Oxford, Oxford, UK

Corresponding authors: Edwina F. Yeo, edwina.yeo.14@ucl.ac.uk;
Benjamin J. Walker, benjamin.walker@ucl.ac.uk;
Philip Pearce, philip.pearce@ucl.ac.uk; Mohit P. Dalwadi, mohit.dalwadi@maths.ox.ac.uk

(Received 12 June 2026 UTC; revised 27 July 2026 UTC; accepted 11 August 2026 UTC)

Minimising bacterial surface adhesion and subsequent biofilm formation in industrial and medical settings requires understanding how bacteria are transported and adhere to complex surface geometries in the presence of non-uniform flow. In this paper, we consider the transport of a dilute suspension of motile bacteria through a corrugated two-dimensional channel with perfectly adhesive walls. Considering flows much faster than the bacterial swimming speed, we asymptotically analyse the diffusive boundary layer that forms using a curvilinear coordinate system based on the fluid streamfunction. We present a similarity solution to the diffusivity-varying diffusion-type equation that arises, from which we derive an analytical expression for the bacterial adhesion rate as a function of surface arclength and the spatially varying wall shear rate. Our model predicts that bacterial adhesion becomes localised on curved surfaces, with bacteria showing preferential adhesion to wall 'peaks' at lower shear rates and preferential adhesion to wall 'valleys' at higher shear rates. More broadly, our results highlight how spatially varying flows generated by complex geometries can lead to localised bacterial adhesion, with potential implications for both enhancing and minimising biofilm formation.

Key words: micro-organism dynamics, active matter, boundary layers

© The Author(s), 2026. Published by Cambridge University Press. This is an Open Access article, distributed under the terms of the Creative Commons Attribution licence (https://creativecommons.org/licenses/by/4.0/), which permits unrestricted re-use, distribution and reproduction, provided the original article is properly cited.

https://doi.org/10.1017/jfm.2026.12022 Published online by Cambridge University Press

1. Introduction

Surface colonisation by bacteria leads to healthcare-associated infections, the fouling of food products and the loss of efficacy of wastewater treatment (Shirtliff & Leid 2009; Cámara *et al.* 2022). Many common pathogens reorient and propel themselves in search of nutrients or surfaces on which they can form a biofilm (Wei *et al.* 2011). This motility means bacteria can exhibit more complex dynamics in flow than passive particles. Even in unidirectional shear flow, bacterial surface adhesion rates have been measured in experiments to either increase or decrease as a function of the fluid shear depending on the experimental set-up (Lecuyer *et al.* 2011; Park *et al.* 2011; Moreira *et al.* 2014; Saur *et al.* 2017; Palalay *et al.* 2023). Recent theoretical analysis of bacterial adhesion in shear flow has predicted a non-monotonic adhesion rate as a function of shear rate in simple channel flow, demonstrating that adhesion is reduced by upstream bacterial reorientation at high flow rates (Yeo *et al.* 2026). However, many medical and industrial systems are associated with more complex geometries with textured surfaces, bends and constrictions. The effects of these geometries on bacterial adhesion have not been theoretically quantified.

The length scale of constrictions, obstacles or textured surfaces relative to the bacterial body size is a key determinant in predicting their effect on bacterial adhesion (Cheng *et al.* 2019). Surface modifications of length scales below $5\,\mu$m can reduce bacterial attachment by actively killing bacteria on contact (Tripathy *et al.* 2017), or by limiting the accessible area available for bacteria to adhere (Pellegrino *et al.* 2026). Large length-scale modifications ($>5\,\mu$m) generate regions of high and low fluid shear, significantly altering the hydrodynamic transport of bacteria. In experiments, this has been found to have different effects on bacterial surface accumulation depending on the size of the wall shear rate compared with the bacterial swimming speed: bacteria accumulate downstream of obstacles or constrictions for relatively low shear rates of $<30\,\mathrm{s}^{-1}$ (Altshuler *et al.* 2013; Miño *et al.* 2018; Secchi *et al.* 2020) and upstream of obstacles at relatively high shear rates of $\approx 200\,\mathrm{s}^{-1}$ (Secchi *et al.* 2020); this transition has been replicated in agent-based models (Secchi *et al.* 2020; Lee *et al.* 2021; Lohrmann & Holm 2023). The transition from downstream to upstream adhesion has been attributed to the reduced effect of bacterial motility as the flow speed increases above the bacterial swimming speed; for passive particles, adhesion would be expected to be higher upstream. For even higher shear rates $\approx 1000\,\mathrm{s}^{-1}$, bacteria have been found to accumulate at the bottom of valleys or cavities, potentially because of increased fluid erosion at peaks (Scheuerman *et al.* 1998; Lee *et al.* 2013). These experimental findings demonstrate that it is challenging to disentangle the competing surface effects of bacterial attachment, boundary shape, fluid erosion and growth in experiments. Therefore, in this paper we will use a theoretical approach to isolate the roles of hydrodynamics and motility in facilitating bacterial attachment to curved surfaces, focusing our analysis on the high-shear environments typical of industrial and medical settings.

The effect of flow on the adhesion of passive particles in straight and curved channels has previously been quantified theoretically. Classical work predicts that increasing flow increases mass transport and, therefore, adhesion; a boundary layer analysis in shear flow yields a surface adhesion rate of $J \sim \dot{\gamma}^{1/3} D^{2/3} x^{-1/3}$, where D is the particle diffusion coefficient, $\dot{\gamma}$ is the wall shear rate and x is the distance from the particle source (Lévêque 1928). An extension of this result to more complex geometries was provided by Lighthill (1950), who analysed thermal boundary layers over general surfaces using an arclength rescaling method. More recently, we theoretically quantified the effects of activity on adhesion in straight channels, predicting that the adhesion rate of motile

https://doi.org/10.1017/jfm.2026.12022 Published online by Cambridge University Press

bacteria with swimming speed $\mathcal{V}_s$ and rotational diffusion coefficient D_r in shear flow depends non-monotonically on the wall shear rate (Yeo *et al.* 2026). This is captured by an effective diffusivity D_{eff}. At low shear, $D_{eff} \sim \mathcal{V}_s^2/2D_r$, in agreement with the quiescent approximation of Berg (1993), giving $J \sim \dot{\gamma}^{1/3}$; at high shear, upstream bacterial reorientation limits diffusivity and, therefore, adhesion, with $J \sim \dot{\gamma}^{-1}$ instead (Yeo *et al.* 2026). Generalising these results to understand active particle adhesion to curved surfaces requires characterising the effective diffusivity of bacterial suspensions in high-speed, spatially varying fluid flows near boundaries.

The diffusivity of bacterial suspensions in the absence of adhesion has predominantly been estimated using generalised Taylor dispersion (GTD) in systems including unidirectional flows (Frankel & Brenner 1991; Bearon 2003), quiescent suspensions in slowly varying corrugated channels (Yariv & Schnitzer 2014) and porous medium flow (Alonso-Matilla *et al.* 2019). An alternative approach to GTD was used in Fung *et al.* (2022), which approximates bacterial dispersion in multidirectional flows using the local flow gradient. However, the large gradients in both density and orientation that form when fluid advection greatly exceeds motility mean that the requisite assumptions of spatial homogeneity used in both GTD and the local approximation model of Fung *et al.* (2022) cannot be used. Hence, the combined effect of strong flow and curved boundaries on bacterial adhesion remains to be quantified theoretically.

In this paper, we consider the perfect adhesion of bacteria to corrugated surfaces in flow (§ 2). Using a curvilinear coordinate system defined via the fluid streamfunction (§ 2.1), we asymptotically analyse the boundary layer that forms in advection-dominated regimes (§ 3). We then derive a similarity solution to the subsequent boundary layer equation using an adaptation of the flow approximation and arclength rescaling in Lighthill (1950). Using this similarity solution, we calculate an analytic expression for the bacterial adhesion rate in terms of the local wall shear rate (§ 3.2). We evaluate this solution using numerical Stokes flow solutions, demonstrating that bacterial adhesion can be localised to either wall 'valleys' or 'peaks' depending on the ratio of the bacterial rotational diffusion to the fluid shear rate (§ 4). By varying the surface geometry we show that bacterial localisation is further exaggerated when the curved walls have tall obstacles with short wavelengths, which most significantly disturb the flow.

2. Problem statement

We consider the steady flow of a dilute suspension of bacteria through a two-dimensional channel defined by $|y| < h(x)$, $0 < x < L$, with corrugated, perfectly absorbing walls at $|y| = h(x)$, as shown in figure 1. Symmetry allows for consideration of only $y \in (-h(x), 0)$. We take the bacteria to be circular rigid bodies that experience rotational diffusion with coefficient D_r and propel themselves with fixed speed $\mathcal{V}_s$ in the direction they are facing. We consider circular bacteria since the role of bacterial shape was found to only have a small effect on adhesion at high shear by Yeo *et al.* (2026). We use the dilute active suspension model presented by Saintillan & Shelley (2014), additionally assuming that the suspension is dilute enough to neglect physical and hydrodynamic interactions between bacteria; the latter assumption implies that the fluid flow is independent of the bacteria.

We present the governing equations in dimensionless form, obtained by the following scalings: length with the maximum half-channel width d; fluid velocity with twice the maximum inlet velocity $2U_{max}$ (where the prefactor of two means that $u \sim y$ near the wall); fluid pressure with the viscous pressure scale $2\mu U_{max}/d$, where μ is the constant fluid

https://doi.org/10.1017/jfm.2026.12022 Published online by Cambridge University Press

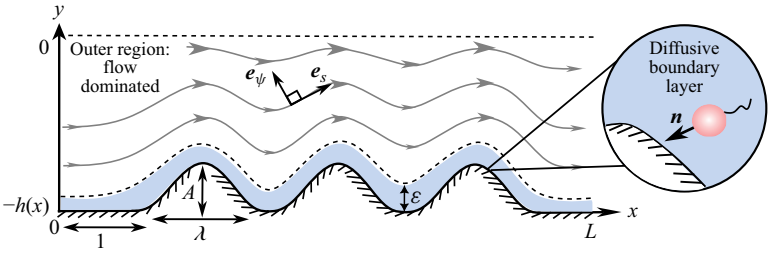


Figure 1. Schematic for flow of a bacterial suspension through a channel with corrugated, absorbing walls. The asymptotic structure is split between the flow-dominated outer region and the diffusive boundary layer near $y = -h(x)$ (shaded blue) with thickness ε, where bacteria are mainly oriented towards the boundary (inset). Lower half of domain $y \in [-h(x), 0]$ shown, with symmetry across $y = 0$. Also shown are: representative fluid streamlines (grey), arclength and streamfunction unit vectors $(\boldsymbol{e}_s, \boldsymbol{e}_\psi)$ and wall geometry amplitude A and wavelength λ.

viscosity; and bacterial density with the (constant) inlet density ρ_i. Under these scalings, the steady Stokes equations apply for the dimensionless fluid velocity field $\boldsymbol{u} = u\boldsymbol{e}_x + v\boldsymbol{e}_y$ (where $\boldsymbol{e}_i$ is the unit vector in the i direction) and pressure p

$$\nabla^2 \boldsymbol{u} = \nabla p, \quad \nabla \cdot \boldsymbol{u} = 0. \tag{2.1}$$

The dimensionless bacterial density ρ, mean orientation vector $\boldsymbol{n}$ and the traceless nematic order tensor $\boldsymbol{Q}$ are governed by the dilute active fluid equations (Saintillan & Shelley 2014, although here we do not include translational diffusion as it is negligible for bacteria)

$$\boldsymbol{u} \cdot \nabla \rho = -V_s \nabla \cdot (\rho \boldsymbol{n}), \tag{2.2}$$

$$\boldsymbol{u} \cdot \nabla (\rho \boldsymbol{n}) = -V_s \left(\nabla \cdot (\rho \boldsymbol{Q}) + \frac{1}{2} \nabla \rho \right) + (\rho \boldsymbol{I}\boldsymbol{n} - \boldsymbol{T}) : \boldsymbol{W} - \frac{\rho \boldsymbol{n}}{Pe_r}, \tag{2.3}$$

$$\boldsymbol{u} \cdot \nabla (\rho \boldsymbol{Q}) = -V_s \left(\nabla \cdot \boldsymbol{T} + \frac{\boldsymbol{I}}{2} \nabla \cdot (\rho \boldsymbol{n}) \right) + \rho (\boldsymbol{W}\boldsymbol{Q} - \boldsymbol{Q}\boldsymbol{W}) - \frac{4\rho \boldsymbol{Q}}{Pe_r}. \tag{2.4}$$

Equations (2.3)–(2.4) capture advection, bacterial swimming and rotation of bacteria by the flow which is proportional to the rate of rotation tensor $\boldsymbol{W} := (\nabla \boldsymbol{u} - \nabla \boldsymbol{u}^{\mathrm{T}})/2$, where $\boldsymbol{I}$ is the identity tensor. Two dimensionless parameters define the bacterial dynamics: $V_s = \mathcal{V}_s / 2U_{max}$, the ratio of the bacterial swimming speed to the flow speed, and $Pe_r = 2U_{max}/d D_r$, the rotational Péclet number, which captures the ratio of fluid rotation to reorientation by diffusion. Equations (2.2)–(2.4) are obtained through successive moments of a Fokker–Planck equation describing the dynamics of a collection of stochastic bacteria. To close this system, higher-order moments must be approximated through the use of a closure. We use the two-dimensional isotropic closure, analogous to a Fourier series in orientation in two dimensions, which defines components of the rank three tensor in (2.3)–(2.4) as $\boldsymbol{T}_{ijk} = \rho(\delta_{ij} n_k + \delta_{ik} n_j + \delta_{jk} n_i)/4$, where δ_{ij} is the Kronecker delta.

Classifying the partial differential equation (PDE) system (2.2)–(2.4) shows that it is hyperbolic almost everywhere in the limit of $V_s \ll 1$ that we consider (near the no-slip boundary there is a very thin region, thinner than the boundary layer we subsequently consider, in which the PDE system becomes of mixed type, through which the leading-order vertical flux is conserved). The direction of the characteristics means that some information propagates from the lower boundary into the domain, allowing us to implement an absorption condition on bacterial density. As we will see subsequently, the following

https://doi.org/10.1017/jfm.2026.12022 Published online by Cambridge University Press

boundary conditions are sufficient to solve the leading-order system we derive. At the inlet ($x = 0$) we impose a fixed bacterial density $\rho = 1$, unbiased swimming direction $\boldsymbol{n} = \boldsymbol{0}$, uniform angular distribution $\boldsymbol{Q} = \boldsymbol{0}$ and a unidirectional, parabolic fluid velocity profile $(u, v) = ((1 - y^2)/2, 0)$. As we approach the lower channel wall ($y \to -h(x)^+$), perfect bacterial absorption implies that $\rho \to 0$ (technically a matching condition), and we additionally impose no slip and no flux: $\boldsymbol{u} = \boldsymbol{0}$. At the channel outlet ($x = L$) we impose unidirectional flow $v = 0$ and atmospheric pressure $p = 0$. At the channel centreline ($y = 0$) we impose symmetry conditions: $v = 0,\ \partial\rho/\partial y = 0,\ \partial u/\partial y = 0$.

In the simulations, the corrugated-channel walls are defined by an initial straight section, then three peaks of variable amplitude A and wavelength λ and a subsequent straight section, which allows the flow to relax back to a unidirectional profile at the outlet located at $x = L$, with $h(x) = 1 - A\sin^2(\pi(x - 1)/\lambda)$ for $1 < x < 3\lambda + 1$ and $h(x) = 1$ otherwise.

2.1. *Arclength–streamfunction coordinate system*

We analyse (2.2)–(2.4) in curvilinear (arclength–streamfunction) coordinates (s, ψ) (as used previously in, e.g. Batchelor (1956), Cummings & Waters (2007), Booth *et al.* (2024)). Here, s describes the arclength along each streamline, with $s = 0$ at $x = 0$, and the fluid streamfunction ψ is defined by $u = \partial\psi/\partial y$, $v = -\partial\psi/\partial x$. This coordinate system has unit vectors $\boldsymbol{e}_s$ and $\boldsymbol{e}_\psi$, which lie tangent and normal to fluid streamlines, respectively (shown in figure 1). By definition, the fluid velocity is purely in the $\boldsymbol{e}_s$ direction, with variable magnitude $|\boldsymbol{u}| = U(s, \psi) > 0$ such that $\boldsymbol{u} = U(s, \psi)\boldsymbol{e}_s$. In this coordinate system, the gradient and divergence operators are

$$\boldsymbol{\nabla} f = \frac{\partial f}{\partial s}\boldsymbol{e}_s + U\frac{\partial f}{\partial \psi}\boldsymbol{e}_\psi, \quad \boldsymbol{\nabla}\cdot\boldsymbol{g} = U\left(\frac{\partial}{\partial s}\left(\frac{g_s}{U}\right) + \frac{\partial(g_\psi)}{\partial\psi}\right) \tag{2.5}$$

for a scalar function f and a vector function $\boldsymbol{g} = g_s\boldsymbol{e}_s + g_\psi\boldsymbol{e}_\psi$, where derivatives with respect to ψ capture shear gradients, and derivatives with respect to s capture flow acceleration along a streamline. We consider corrugated surfaces of moderate curvature for which there are no regions of recirculation, allowing us to uniquely set $\psi = 0$ on $y = -h(x)$.

3. Analytical solution

We consider the regime in which fluid flow is much faster than the swimming speed of an individual bacterium, corresponding to $V_s \ll 1$, in the distinguished limit in which $Pe_r = O(1)$. In this regime, the asymptotic structure of the solution is divided into an outer region where bacteria advect as passive tracers, and an inner (boundary) layer where the complex bacterial dynamics and adhesion alter bacterial density. Conceptually, this structure is similar to the problem of bacterial adhesion past a flat plate (Yeo *et al.* 2026), although here with curved boundaries and multidirectional flow.

3.1. *Flow-dominated outer region*

In the weak-swimming limit $V_s \ll 1$, far from the absorbing boundary at $y = -h(x)$, (2.2) states that bacteria remain on fluid streamlines at leading order, with a constant density $\rho = 1$ set by the inlet condition. Then, the leading-order versions of (2.3) and (2.4) consist of a balance between rotational diffusion, fluid rotation and advection along streamlines

$$U\frac{\partial(\rho\boldsymbol{n})}{\partial s} = (\rho\boldsymbol{I}\boldsymbol{n} - \boldsymbol{T}) : \boldsymbol{W} - \frac{\rho\boldsymbol{n}}{Pe_r}, \qquad U\frac{\partial(\rho\boldsymbol{Q})}{\partial s} = \rho(\boldsymbol{W}\boldsymbol{Q} - \boldsymbol{Q}\boldsymbol{W}) - \frac{4\rho\boldsymbol{Q}}{Pe_r}. \tag{3.1}$$

https://doi.org/10.1017/jfm.2026.12022 Published online by Cambridge University Press

Using the homogeneous inlet conditions, equations (3.1) generate the solutions $\boldsymbol{n} = \boldsymbol{Q} = \boldsymbol{0}$. That is, in the outer region, the bacteria are uniformly oriented with unbiased swimming direction.

3.2. *Boundary layer*

Close to the curved wall, no slip means that the fluid flow slows and eventually becomes comparable to the magnitude of bacterial swimming. When this occurs, a diffusive boundary layer forms where the bacterial density is determined by a balance of streamwise advection and swimming normal to the streamlines. The thickness of this layer, ε, will be identified as part of our subsequent analysis. Since $u \sim y$ near the wall, the flow in this boundary layer is of $O(\varepsilon)$ and, hence, the streamfunction is of $O(\varepsilon^2)$. We consider surfaces with moderate curvature $|\kappa| \ll 1/\varepsilon$. We scale into this boundary layer region by defining a new streamfunction $\psi = \varepsilon^2 \Psi$, fluid velocity $\boldsymbol{u} = \varepsilon \tilde{U} \boldsymbol{e}_s$ and mean orientation $\boldsymbol{n} = \varepsilon^{1/2} \tilde{\boldsymbol{n}}$, denoting other dependent inner variables with tildes. The leading-order scaled version of (2.2) is

$$\varepsilon \tilde{U} \frac{\partial \tilde{\rho}}{\partial s} + \frac{V_s \tilde{U}}{\varepsilon^{1/2}} \frac{\partial (\tilde{\rho} \tilde{n}_\Psi)}{\partial \Psi} = 0. \tag{3.2}$$

Here, $\tilde{\rho}\tilde{n}_\Psi$ captures the proportion of bacteria oriented normal to streamlines. We seek solutions such that swimming balances advection in (3.2), so that $\varepsilon = O(V_s^{2/3})$. Rescaling (2.3), this is achieved by a balance between fluid rotation, rotational diffusion and swimming of bacteria down density gradients in the Ψ-direction, resulting in the leading-order equations

$$0 = \frac{1}{2} \tilde{U} \frac{\partial \tilde{U}}{\partial \Psi} \tilde{\rho} \tilde{n}_\Psi - \frac{\tilde{\rho} \tilde{n}_s}{Pe_r}, \quad 0 = -\frac{1}{2} \tilde{U} \frac{\partial \tilde{U}}{\partial \Psi} \tilde{\rho} \tilde{n}_s - \frac{\tilde{\rho} \tilde{n}_\Psi}{Pe_r} - \frac{V_s \tilde{U}}{2\varepsilon^{3/2}} \frac{\partial \tilde{\rho}}{\partial \Psi}. \tag{3.3}$$

Here, we only see shear gradients of the flow, which are dominant in the boundary layer. We can rewrite (3.3) to determine the components of $\rho \tilde{\boldsymbol{n}}$ in terms of the other variables

$$\tilde{\rho} \tilde{n}_\Psi = -\frac{2 V_s Pe_r \tilde{U}}{\varepsilon^{3/2} \left(Pe_r^2 \tilde{U}^2 \left(\dfrac{\partial \tilde{U}}{\partial \Psi} \right)^2 + 4 \right)} \frac{\partial \tilde{\rho}}{\partial \Psi}, \quad \tilde{\rho} \tilde{n}_s = -\frac{V_s Pe_r^2 \tilde{U} \left(\dfrac{\partial \tilde{U}}{\partial \Psi} \right)^2}{\varepsilon^{3/2} \left(Pe_r^2 \tilde{U}^2 \left(\dfrac{\partial \tilde{U}}{\partial \Psi} \right)^2 + 4 \right)} \frac{\partial \tilde{\rho}}{\partial \Psi}. \tag{3.4}$$

Hence, the scaled mean swimming direction $\tilde{\boldsymbol{n}}$ points down gradients in bacterial density perpendicular to the flow, with magnitude that depends on the local fluid shear. The self-consistent asymptotic scalings suggest that the nematic order tensor is much smaller than the retained terms, so it does not appear in (3.4). Combining (3.2) and (3.4), we obtain a closed (spatially varying diffusion) equation for the leading-order bacterial density

$$\frac{\partial \tilde{\rho}}{\partial s} - \frac{2 V_s^2 Pe_r}{\varepsilon^3} \frac{\partial}{\partial \Psi} \left(\frac{\tilde{U}}{Pe_r^2 \tilde{U}^2 \left(\dfrac{\partial \tilde{U}}{\partial \Psi} \right)^2 + 4} \frac{\partial \tilde{\rho}}{\partial \Psi} \right) = 0, \tag{3.5}$$

https://doi.org/10.1017/jfm.2026.12022 Published online by Cambridge University Press

with boundary conditions $\tilde{\rho} \to 0$ as $\Psi \to 0$ and $\tilde{\rho} \to 1$ as $\Psi \to \infty$. Since $\tilde{U}\partial\tilde{\rho}/\partial\Psi$ remains finite as $\Psi \to 0$, (3.4) shows that $\tilde{\rho}\tilde{n}_\Psi$ remains finite and hence that $\tilde{n}_\Psi$ becomes large (specifically, $|\boldsymbol{n}| = O(1)$) in a thinner boundary layer near $\Psi = 0$. As (3.2) indicates that the vertical flux (our quantity of interest) would remain constant in this thinner region, for brevity we do not consider this thinner boundary layer further. Finally, we note that it is convenient to define the boundary layer thickness by considering the scale of $\tilde{U}$ and $\partial\tilde{U}/\partial\Psi$ in the straight portion of the boundary, giving $\varepsilon^3 = 2V_s^2 Pe_r/(Pe_r^2 + 4)$.

Following Fage & Falkner (1931) and Lighthill (1950) for passive particles, (3.5) admits a similarity solution in the scenario where the boundary layer flow is well approximated by shear flow with dimensionless shear rate $\dot{\gamma}(s)$. In this case, the boundary layer flow can be written as $\tilde{U} = \sqrt{2\dot{\gamma}(s)\Psi} + O(\varepsilon)$ (this reduces to unidirectional shear flow, $\tilde{U} = \sqrt{2\Psi}$, when the surface is flat and $\dot{\gamma}(s) = 1$), and (3.5) becomes

$$\frac{\partial\tilde{\rho}}{\partial s} - \frac{\sqrt{\dot{\gamma}(s)}\left(Pe_r^2 + 4\right)}{\left(Pe_r^2\dot{\gamma}(s)^2 + 4\right)}\frac{\partial}{\partial\Psi}\left(\sqrt{2\Psi}\frac{\partial\tilde{\rho}}{\partial\Psi}\right) = 0. \tag{3.6}$$

Using a nonlinear scaling of the arclength $\xi(s)$, we can transform (3.6) into

$$\frac{\partial\tilde{\rho}}{\partial\xi} - \frac{\partial}{\partial\Psi}\left(\sqrt{2\Psi}\frac{\partial\tilde{\rho}}{\partial\Psi}\right) = 0 \quad \text{with} \quad \xi = \int_0^s \frac{\sqrt{\dot{\gamma}(\hat{s})}\left(Pe_r^2 + 4\right)}{\left(Pe_r^2\dot{\gamma}(\hat{s})^2 + 4\right)}\,\mathrm{d}\hat{s}. \tag{3.7}$$

Then, we obtain a similarity solution to (3.7) using the similarity variable $\eta = \Psi\xi^{-2/3}$. Imposing the appropriate boundary conditions, we obtain the solution

$$\rho(s,\psi) = \frac{1}{\Gamma(1/3)}\Gamma\left(\frac{1}{3}, \frac{4\,\psi^{3/2}}{9\sqrt{2}V_s^2 Pe_r\int_0^s \sqrt{\dot{\gamma}(\hat{s})}\left(Pe_r^2\dot{\gamma}(\hat{s})^2 + 4\right)^{-1}\,\mathrm{d}\hat{s}}\right), \tag{3.8}$$

which we write in terms of the standard (s, ψ) coordinates. In (3.8), $\Gamma(a, z)$ is the lower incomplete gamma function and $\Gamma(a)$ is the gamma function.

The pointwise bacterial surface adhesion rate $J(s)$ is defined by the vertical swimming flux of bacteria, $J(s) = -V_s\rho n_\psi|_{\psi=0}$. Using (3.4) and our analytic solution (3.8), we may derive an analytic expression for the bacterial surface adhesion rate along the curved surface

$$\begin{aligned} J(s) &= \frac{2V_s Pe_r\sqrt{2\dot{\gamma}(s)\psi}}{\left(Pe_r^2\dot{\gamma}(s)^2 + 4\right)}\frac{\partial\rho}{\partial\psi}\bigg|_{\psi=0} \\ &= \frac{3^{1/3}}{\Gamma(1/3)}\frac{(2V_s^2 Pe_r)^{2/3}\sqrt{\dot{\gamma}(s)}}{\left(Pe_r^2\dot{\gamma}(s)^2 + 4\right)}\left(\int_0^s \frac{\sqrt{\dot{\gamma}(\hat{s})}}{\left(Pe_r^2\dot{\gamma}(\hat{s})^2 + 4\right)}\,\mathrm{d}\hat{s}\right)^{-1/3}. \end{aligned} \tag{3.9}$$

Reassuringly, (3.9) reduces to the flat-plate adhesion result of Yeo *et al.* (2026) in the appropriate limit of $\dot{\gamma}(s) = 1$, under the substitutions $s = x$ and $\psi = y^2/2$. We note that (3.8) and (3.9) are asymptotically valid in the region $x = O(1)$, $y + h(x) = O(\varepsilon)$; they do not formally hold near the corner with the discontinuity (where $x = O(\varepsilon)$, $y + h(x) = O(\varepsilon)$), where axial swimming would also be important.

4. Numerical results

We have derived an analytical expression to predict bacterial adhesion to curved surfaces, which requires only the local wall shear rate and the bacterial motility parameters to evaluate via (3.9). The integral in (3.9) describes the cumulative effect of upstream shear and adhesion on the bacterial density, and the remaining terms describe the instantaneous

https://doi.org/10.1017/jfm.2026.12022 Published online by Cambridge University Press

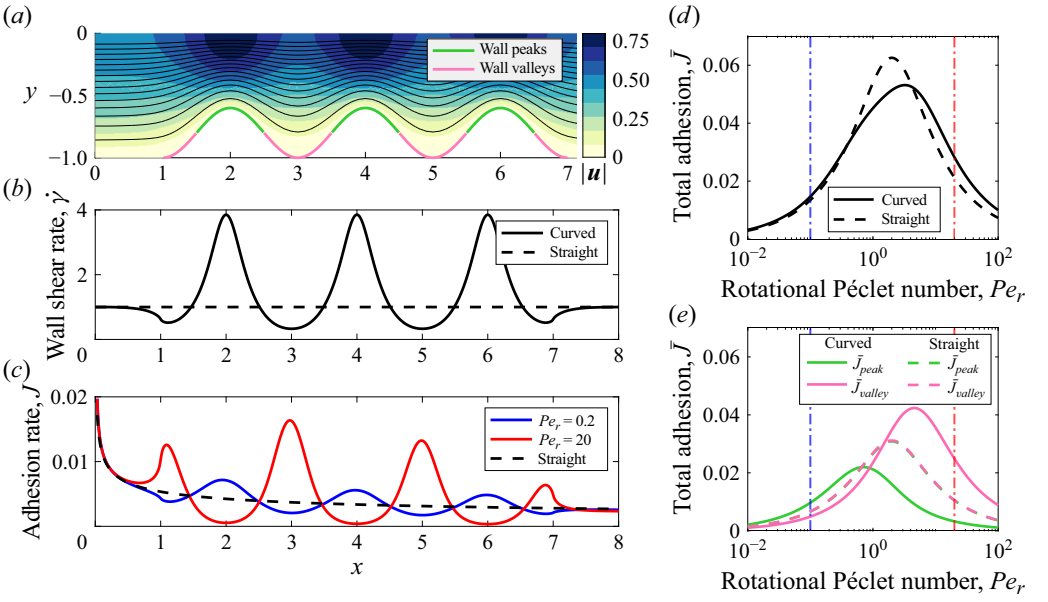


Figure 2. (*a*) Fluid velocity magnitude in corrugated channel with black streamlines overlaid; coloured lines mark wall valleys and peaks. (*b*) Wall shear rate in corrugated and straight channels. (*c*) Spatial adhesion distribution for $Pe_r = 0.2$ and $Pe_r = 20$. (*d*) Total adhesion in corrugated region for a range of Pe_r. (*e*) Total adhesion to peaks and valleys for a range of Pe_r (see panel (*a*) for relevant parts of the boundary). All results are for $V_s = 0.1$ and wall parameters $A = 0.4$, $\lambda = 2$, $L = 12$, with straight channel alternatives shown dashed in (*b–e*). Vertical lines in (*d–e*) correspond to $Pe_r = 0.2$ and 20 as in (*c*).

response of the mean bacterial orientation to local shear rate $\dot{\gamma}(s)$. To evaluate (3.9), we numerically simulate a spatially varying flow through a corrugated channel.

4.1. *Simulation method*

We solve the fluid problem (2.1) with the finite element method implemented using the Python Package FEniCS (Logg & Wells 2010; Logg *et al.* 2012*b*), which allows implementation of the weak form in the language UFL (Kirby & Logg 2006; Ølgaard & Wells 2010; Logg *et al.* 2012*a*). The problem is then compiled by `FIAT` (Kirby 2012). We use `Gmsh` to construct a mesh of the channel geometry (Geuzaine & Remacle 2009). We then solve for the wall shear stress by computing gradients of the fluid solution. For all simulations we take the overall channel length to be $L = 12$, which we find to be sufficiently long for the unidirectional outlet flow boundary condition to not significantly alter the flow.

4.2. *Adhesion rates in corrugated channels*

In the corrugated channel, the wall shear rate is higher at the wall peaks and lower in wall valleys (figures 2*a* and 2*b*). This produces spatially localised bacterial adhesion $J(s)$, with bacteria preferentially adhering to wall peaks at low Pe_r and to wall valleys at high Pe_r (figure 2*c*).

A comparison of our corrugated-channel results with straight channels shows that the total adhesion of bacteria $\bar{J} = \int J\,dx$ in the corrugated region $(1 < x < 1 + 3\lambda)$ can be either reduced or increased by the corrugations (figure 2*d*). At intermediate Péclet numbers ($Pe_r \approx 1$) overall adhesion is reduced by up to 20 %; at lower and higher Pe_r, overall adhesion is increased by up to 35 % (figure 2*d*). Comparing total adhesion to peaks ($\bar{J}_{peak}$)

https://doi.org/10.1017/jfm.2026.12022 Published online by Cambridge University Press

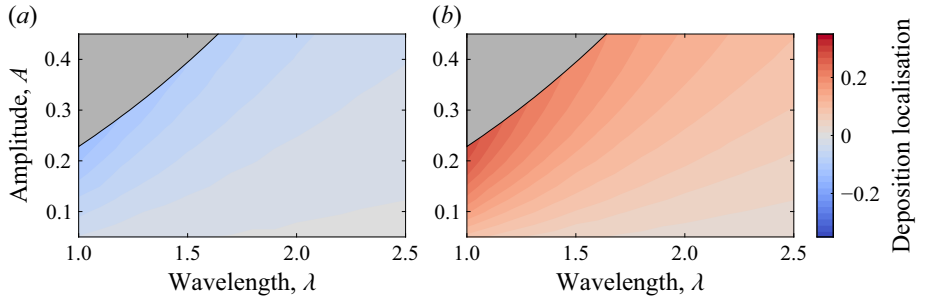


Figure 3. Deposition localisation, quantified by $(\bar{J}_{valley} - \bar{J}_{peak})/(3\bar{J}\lambda)$ for a range of wall parameters with $V_s = 0.1$. (*a*) Negative values show peak localisation at $Pe_r = 0.2$. (*b*) Positive values show valley localisation at $Pe_r = 20$. In both panels the strongest localisation occurs for tall, small-wavelength corrugations. In the grey region, flow in valleys is insufficient to apply asymptotic results (see § 4).

and to valleys ($\bar{J}_{valley}$) further demonstrates localised adhesion (figure 2*e*). This is in contrast to straight channels, for which adhesion varies equally with Pe_r at all locations along the wall.

Varying the wavelength λ and amplitude A of the corrugated walls allows for control of the wall shear rate difference between peaks and valleys. Broadly, larger amplitudes generate greater wall shear rates on the peaks, and smaller wavelengths generate lower wall shear rates in the valleys. The relative localisation per wall wavelength can be quantified by $(\bar{J}_{valley} - \bar{J}_{peak})/(3\bar{J}\lambda)$, which is positive for valley-localised adhesion and negative for peak-localised adhesion (figure 3). We do not consider walls with sufficiently large amplitudes or small wavelengths for which the flow in the valleys becomes slow and eddies are generated (Moffatt 1964); both our assumption of $V_s \ll 1$ and our streamfunction formulation break down in this regime, marked in grey in figure 3. The adhesion is peak localised at low Pe_r (figure 3*a*), and valley localised at high Pe_r (figure 3*b*), although the precise extent of localisation varies with the corrugation parameters. The most extreme localisation occurs for corrugation with tall amplitude and small wavelength, for which the disturbance to the flow is greatest.

We can mechanistically understand the localised adhesion by examining (3.9) at low and high rotational Péclet numbers

$$J(s) \sim \begin{cases} \dfrac{3^{1/3}}{\Gamma(1/3)}\left(\dfrac{V_s^2 Pe_r}{2}\right)^{2/3} \dot{\gamma}(s)^{1/2}\left(\int_0^s \dot{\gamma}(\hat{s})^{1/2} d\hat{s}\right)^{-1/3} & \text{for } Pe_r \ll 1, \\ \dfrac{3^{1/3}}{\Gamma(1/3)}\left(\dfrac{2V_s^2}{Pe_r}\right)^{2/3} \dot{\gamma}(s)^{-3/2}\left(\int_0^s \dot{\gamma}(\hat{s})^{-3/2} d\hat{s}\right)^{-1/3} & \text{for } 1 \ll Pe_r \ll \varepsilon^{-1}. \end{cases} \tag{4.1}$$

Although the adhesion rate $J(s)$ has a complex dependence on the upstream shear rate $\dot{\gamma}(s)$ in (4.1), the local term indicates that adhesion should broadly be expected to increase with local shear rate at low Pe_r and decrease with local shear rate at high Pe_r, as is seen in figure 2. Physically, this is driven by the instantaneous response of the mean swimming strength $\boldsymbol{n}$ to the local wall shear rate, with local increases in flow leading to increased mean swimming speed at low Pe_r but to upstream reorientation at high Pe_r. Furthermore, the bacterial adhesion rate responds more strongly to changes in the wall shear rate at high Pe_r, noting the larger exponent of $\dot{\gamma}(s)$ in (4.1). This generates a greater disparity between $\bar{J}_{valley}$ and $\bar{J}_{peak}$ at high Pe_r, with up to eight times as much adhesion in valleys.

https://doi.org/10.1017/jfm.2026.12022 Published online by Cambridge University Press

As expected, the low-Pe_r limit in (4.1) has the same functional dependence on $\dot{\gamma}$ as the heat flux solution in Lighthill (1950), since the bacteria adhere to the surface like passive particles in this limit.

5. Discussion and conclusion

Our findings suggest that adding corrugation to straight devices can control initial bacterial adhesion locations and reduce total adhesion at certain flow rates. Furthermore, our results predict that the initial attachment locations of bacterial species with differing motility parameters could be separated, with some attaching to low-shear valleys and others to high-shear peaks. In practice, overall surface colonisation is the result of both attachment and detachment. Fluid flow has been shown to both increase bacterial detachment, as shear forces overcome attachment (Busscher & Van Der Mei 2006), but also to decrease attachment for specific bacterial surface bonds (FimH in *Escherichia coli* (Sauer *et al.* 2016)) and cell shapes (*Pseudomonas aeruginosa* (Sauer *et al.* 2016)). This difference in post-attachment bacterial response to fluid flow could allow for further control of the biofilm formation process. For example, if shear-enhanced detachment is combined with peak localisation, then overall colonisation would be reduced. However, if shear-enhanced detachment is combined with valley localisation, this could create sheltered zones for bacteria to grow.

Our analysis could be extended to consider elongated bacteria, which have previously been shown to migrate more efficiently in shear flow (Bearon & Durham 2023) and become trapped near boundaries in pipe flow (Rusconi *et al.* 2014). However, the generalised version of (3.5) would feature additional advection terms generated by a non-zero nematic order tensor, so the self-similar scaling could not be applied directly. Scenarios where bacteria adhere imperfectly could be considered by imposing alternative boundary conditions on the walls, see Maretvadakethope *et al.* (2023). Our results were derived using the isotropic closure for the tensor $\boldsymbol{T}$ in (2.3)–(2.4); alternative model closures could offer more accuracy when alignment becomes strong at larger rotational Péclet numbers, but may affect tractability. Although we have used Stokes flow solutions to calculate the analytical bacterial adhesion rate (3.9), our results could be applied to flows with non-zero inertia provided that the flow is well approximated by local shear flow in the diffusive boundary layer. This can hold as long as the viscous boundary layer is much larger than the diffusive one, namely if the reduced Reynolds number $\varepsilon^2\mathrm{Re}$ is small. For instance, considering the transport of the common pathogen *E. coli* with motility parameters $\mathcal{V}_s = 22\ \mu\mathrm{m\,s^{-1}}$, $D_r = 1\ \mathrm{s^{-1}}$(Drescher *et al.* 2011; Saragosti *et al.* 2012) the asymptotic conditions of $V_s \ll 1$, $1 \ll Pe_r \ll \varepsilon^{-1}$ and $\varepsilon^2 Re \ll 1$ mean our results can be applied for flow speeds $11\ \mu\mathrm{m\,s^{-1}} \ll U_{max} \ll 1\ \mathrm{mm\,s^{-1}}$ given a channel half-width of $d = 100\ \mu\mathrm{m}$. Finally, we note that the boundary layers here grow downstream, with height proportional to the cube root of arclength (s). Hence, for long channels the boundary layers eventually merge to form a new asymptotic region when $s = O(\varepsilon^{-3}) = O(V_s^{-2})$, and the bacterial density in the channel bulk becomes non-uniform.

In summary, this work quantifies the role of curved geometry on bacterial surface attachment in flows with speeds much greater than the bacterial swimming speed, demonstrating that non-uniform surface shear can induce localised bacterial adhesion at regions of both higher or lower shear, depending on the scenario of interest. Our focus on advection-dominated flows allows this work to have implications for applications including urinary catheters, food processing facilities and waste water treatment.

https://doi.org/10.1017/jfm.2026.12022 Published online by Cambridge University Press

Funding. E.F.Y. is supported by an EPSRC National Fellowship in Fluid Dynamics (EP/X027902/1). P.P. was supported by a UK Research and Innovation (UKRI) Future Leaders Fellowship (MR/V022385/1, UKRI2746).

Declaration of interests. The authors report no conflict of interest.

Data availability statement. Code available at: https://github.com/Edwina-Yeo/bacterial-curved-adhesion.

References

ALONSO-MATILLA, R., CHAKRABARTI, B. & SAINTILLAN, D. 2019 Transport and dispersion of active particles in periodic porous media. *Phys. Rev. Fluids* **4** (4), 043101.

ALTSHULER, E., MINO, G., PÉREZ-PENICHET, C., DEL RÍO, L., LINDNER, A., ROUSSELET, A. & CLÉMENT, E. 2013 Flow-controlled densification and anomalous dispersion of *E. coli* through a constriction. *Soft Matt.* **9** (6), 1864–1870.

BATCHELOR, G.K. 1956 On steady laminar flow with closed streamlines at large Reynolds number. *J Fluid Mech.* **1** (2), 177–190.

BEARON, R.N. 2003 An extension of generalized Taylor dispersion in unbounded homogeneous shear flows to run-and-tumble chemotactic bacteria. *Phys. Fluids* **15** (6), 1552–1563.

BEARON, R.N. & DURHAM, W.M. 2023 Elongation enhances migration through hydrodynamic shear. *Phys. Rev. Fluids* **8** (3), 033101.

BERG, H.C. 1993 *Random Walks in Biology*. Princeton University Press.

BOOTH, G., DALWADI, M.P., YE, H., MOUTHUY, P.-A. & WATERS, S.L. 2024 Optimal metabolite transport in hollow fibre membrane bioreactors. *Flow* **4**, E18.

BUSSCHER, H.J. & VAN DER MEI, H.C. 2006 Microbial adhesion in flow displacement systems. *Clin. Microbiol. Rev.* **19** (1), 127–141.

CHENG, Y., FENG, G. & MORARU, C.I. 2019 Micro-and nanotopography sensitive bacterial attachment mechanisms: a review. *Front. Microbiol.* **10**, 191.

CUMMINGS, L.J. & WATERS, S.L. 2007 Tissue growth in a rotating bioreactor. Part II: fluid flow and nutrient transport problems. *Math. Med. Biol.* **24** (2), 169–208.

CÁMARA, M., GREEN, W., MACPHEE, C.E., RAKOWSKA, P.D., RAVAL, R., RICHARDSON, M.C., SLATER-JEFFERIES, J., STEVENTON, K. & WEBB, J.S. 2022 Economic significance of biofilms: a multidisciplinary and cross-sectoral challenge. *NPJ Biofilms Microbiomes* **8** (1), 42.

DRESCHER, K., DUNKEL, J., CISNEROS, L.H., GANGULY, S. & GOLDSTEIN, R.E. 2011 Fluid dynamics and noise in bacterial cell–cell and cell–surface scattering. *Proc. Natl Acad. Sci. USA* **108** (27), 10940–10945.

FAGE, A. & FALKNER, V.M. 1931 *Further Experiments on the Flow Around a Circular Cylinder*. Aero Res Committee Rep & Memoranda.

FRANKEL, I. & BRENNER, H. 1991 Generalized Taylor dispersion phenomena in unbounded homogeneous shear flows. *J. Fluid Mech.* **230**, 147–181.

FUNG, L., BEARON, R.N. & HWANG, Y. 2022 A local approximation model for macroscale transport of biased active Brownian particles in a flowing suspension. *J. Fluid Mech.* **935**, A24.

GEUZAINE, C. & REMACLE, J.-F. 2009 Gmsh: a 3-D finite element mesh generator with built-in pre-and post-processing facilities. *Intl J. Numer. Meth. Engng* **79** (11), 1309–1331.

KIRBY, R.C. 2012 FIAT: numerical construction of finite element basis functions. In *Automated Solution of Differential Equations by the Finite Element Method* (ed. A. Logg, K.-A. Mardal & G.N. Wells), vol. 84, chap. 13. Lecture Notes in Computational Science and Engineering. Springer.

KIRBY, R.C. & LOGG, A. 2006 A compiler for variational forms. *ACM Trans. Math. Softw.* **32** (3), 417–444.

LECUYER, S., RUSCONI, R., SHEN, Y., FORSYTH, A., VLAMAKIS, H., KOLTER, R. & STONE, H.A. 2011 Shear stress increases the residence time of adhesion of *Pseudomonas aeruginosa*. *Biophys. J.* **100** (2), 341–350.

LEE, M., LOHRMANN, C., SZUTTOR, K., AURADOU, H. & HOLM, C. 2021 The influence of motility on bacterial accumulation in a microporous channel. *Soft Matt.* **17** (4), 893–902.

LEE, Y.K., WON, Y.-J., YOO, J.H., AHN, K.H. & LEE, C.-H. 2013 Flow analysis and fouling on the patterned membrane surface. *J. Membr. Sci.* **427**, 320–325.

LIGHTHILL, M.J. 1950 Contributions to the theory of heat transfer through a laminar boundary layer. *Proc. R. Soc. Lond. A Math. Phys. Sci.* **202** (1070), 359–377.

LOGG, A. & WELLS, G.N. 2010 DOLFIN: automated finite element computing. *ACM Trans. Math. Softw.* **37** (2), 20.

LOGG, A., ØLGAARD, K.B., ROGNES, M.E. & WELLS, G.N. 2012*a* FFC: the FEniCS form compiler. In *Automated Solution of Differential Equations by the Finite Element Method* (ed. A. Logg, K.-A. Mardal & G.N. Wells), vol. 84, chap. 11. Springer.

https://doi.org/10.1017/jfm.2026.12022 Published online by Cambridge University Press

LOGG, A., WELLS, G.N. & HAKE, J. 2012*b* DOLFIN: a C++/Python finite element library. In *Automated Solution of Differential Equations by the Finite Element Method, Lecture Notes in Computational Science and Engineering* (ed. A. Logg, K.-A. Mardal & G.N. Wells), vol. 84, chap. 10. Springer.

LOHRMANN, C. & HOLM, C. 2023 A novel model for biofilm initiation in porous media flow. *Soft Matt.* **19** (36), 6920–6928.

LÉVÊQUE, A. 1928 *Les lois de la transmission de chaleur par convection*. Dunod.

MARETVADAKETHOPE, S., HAZEL, A.L., VASIEV, B. & BEARON, R.N. 2023 The interplay between bulk flow and boundary conditions on the distribution of microswimmers in channel flow. *J. Fluid Mech.* **976**, A13.

MIÑO, G.L., BAABOUR, M., CHERTCOFF, R., GUTKIND, G., CLÉMENT, E., AURADOU, H. & IPPOLITO, I. 2018 *E. coli* accumulation behind an obstacle. *Adv. Microbiol.* **8** (6), 451–464.

MOFFATT, H.K. 1964 Viscous and resistive eddies near a sharp corner. *J. Fluid Mech.* **18** (1), 1–18.

MOREIRA, J.M.R., ARAÚJO, J.D.P., MIRANDA, J.M., SIMÕES, M., MELO, L.F. & MERGULHÃO, F.J. 2014 The effects of surface properties on *Escherichia coli* adhesion are modulated by shear stress. *Colloids Surf. B Biointerfaces* **123**, 1–7.

ØLGAARD, K.B. & WELLS, G.N. 2010 Optimisations for quadrature representations of finite element tensors through automated code generation. *ACM Trans. Math. Softw.* **37** (1), 8.

PALALAY, J.-J.S., SIMSEK, A.N., REED, J.L., KOCH, M.D., SABASS, B. & SANFILIPPO, J.E. 2023 Shear force enhances adhesion of *Pseudomonas aeruginosa* by counteracting pilus-driven surface departure. *Proc. Natl Acad. Sci. USA* **120** (41), e2307718120.

PARK, A., JEONG, H.-H., LEE, J., KIM, K.P. & LEE, C.-S. 2011 Effect of shear stress on the formation of bacterial biofilm in a microfluidic channel. *BioChip J.* **5**, 236–241.

PELLEGRINO, L., *et al.* 2026 Reduction of bacterial colonization on buckling-induced wrinkled surfaces under fluid shear. *Nat. Commun.* **17**, 1324.

RUSCONI, R., GUASTO, J.S. & STOCKER, R. 2014 Bacterial transport suppressed by fluid shear. *Nat. Phys.* **10** (3), 212–217.

SAINTILLAN, D. & SHELLEY, M.J. 2014 Theory of active suspensions. In *Complex Fluids in Biological Systems: Experiment, Theory, and Computation* (ed. S.E. Spagnolie). Springer.

SARAGOSTI, J., SILBERZAN, P. & BUGUIN, A. 2012 Modeling *E. coli* tumbles by rotational diffusion. implications for chemotaxis. *PLoS One* **7** (4), e35412.

SAUER, M.M., JAKOB, R.P., ERAS, J., BADAY, S., ERIŞ, D., NAVARRA, G., BERNECHE, S., ERNST, B., MAIER, T. & GLOCKSHUBER, R. 2016 Catch-bond mechanism of the bacterial adhesin FimH. *Nat. Commun.* **7** (1), 10738.

SAUR, T., MORIN, E., HABOUZIT, F., BERNET, N. & ESCUDIÉ, R. 2017 Impact of wall shear stress on initial bacterial adhesion in rotating annular reactor. *PLoS One* **12** (2), e0172113.

SCHEUERMAN, T.R., CAMPER, A.K. & HAMILTON, M.A. 1998 Effects of substratum topography on bacterial adhesion. *J. Colloid Interface Sci.* **208** (1), 23–33.

SECCHI, E., VITALE, A., MIÑO, G.L., KANTSLER, V., EBERL, L., RUSCONI, R. & STOCKER, R. 2020 The effect of flow on swimming bacteria controls the initial colonization of curved surfaces. *Nat. Commun.* **11**.

SHIRTLIFF, M. & LEID, J. 2009 *The Role of Biofilms in Device-Related Infections*. Springer.

TRIPATHY, A., SEN, P., SU, B. & BRISCOE, W.H. 2017 Natural and bioinspired nanostructured bactericidal surfaces. *Adv. Colloid Interface Sci.* **248**, 85–104.

WEI, Y., WANG, X., LIU, J., NEMEMAN, I., SINGH, A.H., WEISS, H. & LEVIN, B.R. 2011 The population dynamics of bacteria in physically structured habitats and the adaptive virtue of random motility. *Proc. Natl Acad. Sci. USA* **108** (10), 4047–4052.

YARIV, E. & SCHNITZER, O. 2014 Ratcheting of Brownian swimmers in periodically corrugated channels: a reduced Fokker–Planck approach. *Phys. Rev. E* **90** (3), 032115.

YEO, E.F., WALKER, B.J., PEARCE, P. & DALWADI, M.P. 2026 A shear-induced limit on bacterial surface adhesion in fluid flow. *Proc. Natl Acad. Sci. USA* **123** (4), e2516069123.

https://doi.org/10.1017/jfm.2026.12022 Published online by Cambridge University Press